



Published in final edited form as:

Med Image Anal. 2009 October ; 13(5): 773–784. doi:10.1016/j.media.2009.07.006.

Modelling passive diastolic mechanics with quantitative MRI of cardiac structure and function

Vicky Y. Wang^{a,*}, H.I. Lam^a, Daniel B. Ennis^b, Brett R. Cowan^c, Alistair A. Young^a, and Martyn P. Nash^a

^aAuckland Bioengineering Institute, University of Auckland, Level 6, UniServices House, 70 Symonds Street, Auckland 1142, New Zealand ^bDepartment of Radiological Sciences Diagnostic Cardiovascular Imaging Section, University of California, Peter V. Ueberroth Building, Suite 3371, 10945 LeConte Avenue, Los Angeles, CA 90095-7206, USA ^cCentre for Advanced MRI, University of Auckland, 85 Grafton Road, Auckland 1142, New Zealand

Abstract

The majority of patients with clinically diagnosed heart failure have normal systolic pump function and are commonly categorized as suffering from diastolic heart failure. The left ventricle (LV) remodels its structure and function to adapt to pathophysiological changes in geometry and loading conditions, which in turn can alter the passive ventricular mechanics. In order to better understand passive ventricular mechanics, a LV finite element (FE) model was customized to geometric data segmented from in vivo tagged magnetic resonance images (MRI) data and myofibre orientation derived from ex vivo diffusion tensor MRI (DTMRI) of a canine heart using nonlinear finite element fitting techniques. MRI tissue tagging enables quantitative evaluation of cardiac mechanical function with high spatial and temporal resolution, whilst the direction of maximum water diffusion in each voxel of a DTMRI directly corresponds to the local myocardial fibre orientation. Due to differences in myocardial geometry between in vivo and ex vivo imaging, myofibre orientations were mapped into the geometric FE model using host mesh fitting (a free form deformation technique). Pressure recordings, temporally synchronized to the tagging data, were used as the loading constraints to simulate the LV deformation during diastole. Simulation of diastolic LV mechanics allowed us to estimate the stiffness of the passive LV myocardium based on kinematic data obtained from tagged MRI. Integrated physiological modelling of this kind will allow more insight into mechanics of the LV on an individualized basis, thereby improving our understanding of the underlying structural basis of mechanical dysfunction under pathological conditions.

Keywords

Cardiac magnetic resonance imaging (MRI); Diffusion tensor MRI (DTMRI); Left ventricular (LV) mechanics; Finite element modelling; Material parameter estimation

*Corresponding author. Tel.: +64 9 373 7599x84651; fax: +64 9 367 7157., vicky.wang@auckland.ac.nz (V.Y. Wang).

1. Introduction

More than half of the patients diagnosed with heart failure have normal systolic pump function (e.g. normal ejection fraction) and are thus commonly categorized as suffering from diastolic heart failure (Wang and Nagueh, 2009). Diastolic heart failure is characterized by preserved systolic function, left ventricular (LV) dimensions, and LV volumes, but also by increased LV wall thickness and sometimes LV mass. Changes in physiological, geometrical and/or haemodynamic loading conditions can lead to regional ventricular wall thickening and enhancement or degradation of regional muscle function. This remodelling process results in changes in muscle stiffness during filling, which is an important determinant of global and regional performance of the heart. Given that many patients suffering from heart failure exhibit diastolic dysfunction at an early stage of their condition, passive muscle stiffness has been the focus of much research in cardiac mechanics modelling (Glass et al., 1991).

1.1. Modelling myocardial mechanics

Ventricular myocardium has a complicated three-dimensional (3D) structure, which gives rise to anisotropic, nonlinear and time-dependent material behaviour. Previous attempts to characterize the material properties of myocardium included deducing myocardial resting material properties from the end-diastolic pressure–volume relation and information on regional wall geometry (Costa et al., 2001); or performing in vitro uni-axial or bi-axial tissue testing (Demer and Yin, 1983). Extended bi-axial testing involves orthogonal loading of thick rectangular tissue slices cut parallel to the epicardial surface. After performing bi-axial tests of excised passive myocardium, Demer and Yin (1983) concluded that resting myocardium can be modelled as a nonlinear finite deformation hyperelastic material. However, such tests fail to characterize the 3D in vivo constitutive properties of the heart, and the effects of tissue disruption (as a result of sectioning samples for uni-axial or bi-axial tests) are not well understood (Costa et al., 2001).

Guccione et al. (1991) introduced an inverse modelling approach in cardiac biomechanics to identify constitutive parameters of a transversely-isotropic material relation by analyzing the inflation, stretch and twist of a thick-walled cylinder representative of the equatorial region of a canine LV. Estimation of material properties requires two main fields of data: stress and strain. The latter can be directly measured with the aid of imaging techniques, but the stress field can only be predicted by a reliable computational model. Guccione et al. (1991) quantified the passive constitutive properties of myocardium by matching epicardial strains measured in isolated arrested canine hearts to simulated strains predicted by a model subject to the measured loading conditions. However, experiments using isolated hearts may not be representative of the in vivo passive mechanics and precludes estimation of active mechanics.

In order to accurately study in vivo cardiac constitutive behaviour and the effects of cardiac disease on the passive material properties of the heart, the following information is required:

1. Geometry – represented by customized anatomical heart models consisting of accurate in vivo heart geometry and muscle fibre orientations.

2. Kinematics – detailed recordings of in vivo regional heart wall motion derived from imaging experiments.
3. Boundary conditions – descriptions of the loading conditions and kinematic constraints on the heart.
4. Constitutive relations – describing the nonlinear and anisotropic relationship between stress and strain of the myocardium.

The objective of this study was to develop a modelling framework that integrates detailed measures of in vivo ventricular geometry, motion (kinematics) and pressure measurements (boundary conditions) with ex vivo myofibre orientations to estimate passive mechanical (constitutive) properties of the heart by matching computational estimates of LV wall motion with experimentally recorded myocardial displacements.

1.2. Imaging approaches in cardiac mechanics

Cardiac magnetic resonance imaging (MRI) has become the gold standard for non-invasively quantifying global in vivo heart function with measures such as ejection fraction, cavity volume and mass. Conventional MR techniques, however, are neither capable of quantitatively measuring regional cardiac function nor regional wall motion. The development of tissue tagging MRI has provided a means for quantitatively investigating regional heart motion and the effects of cardiac disease with high spatial and temporal resolution (Axel and Dougherty, 1989; Zerhouni et al., 1988). MRI tissue tagging is a technique that saturates parallel bands of tissue, thus creating high contrast image features that track with heart wall deformation throughout the cardiac cycle. Reconstruction of the 3D motion of the heart from the tag positions during the cardiac cycle requires specialized image processing and mathematical techniques. This procedure often involves combining information from different tagging sets using spatio-temporal interpolation. The final result is a 3D Lagrangian displacement field for the beating heart. Tracked deformation patterns provide non-invasive quantitative information on the mechanical function of the underlying tissue (Young, 1995).

While MR tissue tagging techniques provide detailed cardiac kinematic information, diffusion tensor magnetic resonance imaging (DTMRI) measures the preferred orientations of the local self-diffusion of water molecules in biological tissues. Studies have shown that the direction of maximum diffusion (the primary eigenvector) correlates with the local myofibre orientation observed from histological studies (Hsu et al., 1998; Scollan et al., 1998). Therefore, DTMRI can be used to map the 3D orientations of the myocardial fibres throughout the heart. Myofibre orientation information defines the predominant axis for both mechanical and electrophysiological function, and is therefore essential for modelling both the mechanical behaviour of myocardium and for determining electrical conduction (LeGrice et al., 1995; Ubbink et al., 2006). Myofibre orientations not only exhibit large regional and transmural variation (Ennis et al., 2008), but also remodel as a consequence of disease (Maron et al., 1981). These changes may have direct mechanical and/or electrical ramifications for the heart and lead to mechanical dysfunction and/or arrhythmia. Therefore, a rational approach for studying ventricular biomechanics is to incorporate accurate DTMRI techniques into FE models of cardiac kinematics.

1.3. Myocardial material parameter estimation

Augenstein et al. (2005) developed methods for integrating MRI tagging, DTMRI and pressure recordings in ex vivo passive ventricular inflation experiments. That study primarily focused on the estimation of constitutive parameters of an isolated arrested porcine heart using tagged MRI with simultaneous pressure recordings. Augenstein et al. (2005) proposed a finite element (FE) modelling approach to investigate deformation and stress given the loading and boundary conditions acting on the arrested heart. The 3D deformation field was subsequently constructed from the tagged MRI data, and material parameters were estimated by matching these observed deformations with the FE model predictions for the same heart. Like previous work on estimation of material properties using isolated hearts, this technique may not include all modes of deformation of the heart due to limited deformation under passive loading. Consequently, some material properties of the constitutive equation may be under constrained (Augenstein et al., 2005). Walker et al. (2008) proposed a similar integrative FE model-based analysis method to estimate myocardial constitutive parameters by matching FE predicted strain fields with estimates from tagged MRI.

In this study, we combine in vivo tagging and concurrent pressure recordings with ex vivo DTMRI in a canine heart, using data acquired at the National Institutes of Health in collaboration with Johns Hopkins University (Ennis, 2004). A FE geometric model of the LV was constructed using segmented epicardial and endocardial surface data points from the tagged MRI data. A host mesh fitting approach was used to transform the fibre orientation data derived from the DTMRI to the LV geometric model. Using this integrated model, a finite deformation elasticity problem was solved for early diastolic filling to simulate the passive mechanics of the LV. In our previous study (Wang et al., 2008), we estimated mechanical stiffness by matching end-diastolic LV cavity volume. In this study, we have extended the estimation process to match the predicted localised motion of a large set of embedded material points with that derived from tagged MRI.

This model-based framework integrates information from different imaging and modelling techniques and allows the study of global and regional function and mechanical behaviour of the ventricles. The long-term goals of this research are to gain a better understanding of the underlying structural basis of ventricular mechanics, and to apply these techniques to medical images in order to assist clinicians with the diagnosis and treatment of patients suffering from diastolic heart failure.

2. Methods

2.1. In vivo tagged magnetic resonance imaging

All studies were approved by the local Institutional Review Boards, and conformed to the “Guide for the Care and Use of Laboratory Animals” published by the National Institutes of Health (NIH publication no. 85–23, revised 1985).

Tagged MRI was performed using a General Electric 1.5T CV/i scanner and a 4-element phased array knee coil. Short-axis tagged images (Fig. 1a and b) were acquired using the 3D fast gradient echo pulse sequence with the following parameters: 180 mm × 180 mm × 128–160 mm field of view (FOV), 384 × 128 × 32 acquisition matrix, 12° imaging flip angle,

± 62.5 kHz bandwidth, TE/TR = 3.4/8.0 ms, five pixel tag spacing, and 5 mm slice thickness. Long-axis tags were oriented radially and a 2D fast gradient echo pulse sequence was used to acquire images with parameters: 200 mm \times 200 mm \times 8 mm FOV, 256 \times 128 acquisition matrix, 12° imaging flip angle, ± 31.25 kHz bandwidth, TE/TR = 3.2/8.0, one view per segment, and seven pixel spacing (Ennis, 2004). The narrow tag spacing (2.5 mm) in the short-axis images allow for the direction calculation of radial strains (Fig. 1).

2.2. Ex vivo diffusion tensor MRI

DTMRI was performed following the MR tagging study. The heart was excised and fixed in the end-diastolic configuration and DTMRI data were acquired using the same General Electric 1.5T CV/i scanner and a 4-element phased array knee coil. The imaging protocol used in the experiment was adapted from Helm et al. (2006). Diffusion weighting gradients were incorporated into a 3D fast spin echo sequence. Imaging parameters were as follows: 100 mm \times 100 mm \times 86.4 mm FOV, 128 \times 128 \times 96 acquisition matrix resulting in 780 μ m \times 780 μ m \times 900 μ m voxels, TR/TE (multiple-echo readout) = 600 ms/(62 ms, 72 ms). Diffusion tensor data were reconstructed from the diffusion weighted images (Fig. 2) using linear regression of the logarithm of echo intensities and components of the b -value matrix. The maximum diffusion eigenvector was calculated in each voxel of the DTMRI dataset.

Streeter et al. (1969) reported transmural variation in the fibre angle in the canine heart, whilst more recent measures have demonstrated statistically significant regional differences in fibre angles (Ennis et al., 2008). The distinct transmural changes in myofibre orientation can be clearly seen when visualizing the maximum diffusion eigenvectors derived from the diffusion weighted images (Fig. 3). The primary principal eigenvector rotates in a left-handed helix from approximately -65° on the epicardium, through approximately 0° in the midwall region, to approximately 70° on the endocardium. Fibres located in the most-inner endocardial regions represented papillary muscles or trabecular tissues that were not included in the final geometric model. DTMRI non-destructively provides an accurate description of the fixed heart's myofibre orientations. In this study, we have developed a model-based registration technique to fuse geometric and kinematic data (from tagged MRI) with myocardial microstructural data (from DTMRI) into a biophysical model.

2.3. Image segmentation

LV surface segmentation of the reference (end isovolumic relaxation) tagged MRI images was performed using the Zinc Digitizer.¹ The image frames corresponding to the reference (zero pressure) state and the end-diastolic state of the heart was defined from a long-axis image in which the mitral valve was clearly visible in cross-section. The frame number for which the mitral valve opened was defined as the reference state and the frame at which the mitral valve closed was defined as end-diastole. This same frame number was used for all image series (i.e. all long-axis and short-axis sets of tagged images). For this study, only short-axis images were used for surface contour segmentation. The position of the model apex was determined from the long-axis images. Prior to segmentation, short-axis tagged images were aligned in a cardiac coordinate system (with x orientated along the long-axis of

¹<http://www.cmiss.org/cmgui/zinc>.

the LV, y directed from the centroid of left ventricle to the centroid of the right ventricle, and z directed from anterior to posterior) so that contour points could be readily used for LV geometric fitting (Fig. 4). For this study, the surface contours were defined to exclude the papillary muscles and large trabeculae.

LV surface contours of the DTMRI were also segmented using the Zinc Digitizer. Unlike the tagged MR images, DTMR images were all in the short-axis view and segmentation was performed in a 2D image coordinate system. The segmented surface contour for each short-axis slice was used to create a mask to exclude the pixels outside of the LV myocardium (Fig. 5). To create the myocardial mask, epicardial and endocardial contour points for each slice were interpolated using splines. The intensity of any pixels lying between the two contours was assigned 1 and the remaining pixels were assigned 0. This binary mask was then multiplied with the original DTMRI images. To ensure background pixels at the edge of the myocardium were excluded from the study, the masks for the DTMRI images were eroded by one pixel.

2.4. Left ventricular finite element model creation

A mathematical model of the LV is the key to this framework, because it can combine in vivo geometric information and ex vivo microstructural information of the same heart. We created a FE LV model using nonlinear geometric fitting to match segmented contours of the MR tagged images (Fig. 4). The geometric model consisted of 16 smoothly continuous tri-cubic Hermite finite elements (Bradley et al., 1997), which included four circumferential elements, four longitudinal elements and one transmural element (Fig. 6a and b). The model consisted of 34 nodes and 816 degrees of freedom (DOFs). However, only surface fitting was carried out, thus the number of DOFs was reduced by half. A material coordinate system was also defined such that it was attached to material points and moved with the myocardium as it deformed. Finite element material coordinates (ξ_1, ξ_2, ξ_3) were arranged such that ξ_1 was aligned with the circumferential direction, ξ_2 with the longitudinal (apex-to-base) direction, and ξ_3 with the transmural (endo-to-epi) direction (Fig. 6c).

The endocardial and epicardial surfaces of model were fitted to the corresponding segmented surface data using a least squares approach (Nielsen, 1987) implemented in the modelling software, CMISS.² During the surface fitting, we firstly projected endocardial and epicardial data points to their respective surfaces. We then minimized the mean squared Euclidean distance between the data points (X_{Dn}, Y_{Dn}, Z_{Dn}) and their model projections (X_{Pn}, Y_{Pn}, Z_{Pn}). The squared Euclidean distance for the n th data point projection is defined in Eq. (1).

$$e_n^2 = (x_{Dn} - x_{Pn})^2 + (y_{Dn} - y_{Pn})^2 + (z_{Dn} - z_{Pn})^2 \quad (1)$$

The objective function involved in the geometric fitting procedure is the sum of data projection errors given by:

²<http://www.cmiss.org>.

$$E = \sum_{n=1}^N e_n^2 \quad (2)$$

where N is the total number of data points. Note that the projections were updated during the iterative nonlinear optimisation process.

As the total error was minimized, nodal parameters were modified accordingly, and their final values constituted the optimised geometric model. The goodness of fit was assessed using the root mean square error (RMSE) defined as $\text{RMSE} = \sqrt{E/N}$.

3. Embedding myocardial fibre orientation

Due to the different in vivo versus ex vivo imaging conditions, the shape of the heart obtained from tagged MRI was different to the heart geometry obtained from DTMRI (see Fig. 7a for illustration). The short and long axes dimensions were markedly different between the two image data sets. Moreover, the through-plane resolution was markedly different, with the thickness of the image slices for the tagged MRI and DTMRI being 4 mm and 0.8 mm, respectively. Consequently, image based non-rigid registration (Helm et al., 2005) between the two data sets was not applicable given the substantially altered appearance and comparatively low through-plane resolution of the tagged MRI.

In order to ensure that the geometries defined by the DTMRI and the tagged MRI were consistent before myofibre orientation was incorporated into the finite element model, host mesh fitting (a free form deformation method) was implemented. Host mesh fitting techniques are commonly used to customize generic models to specific cases using a set of identified landmark points and target points. In this study, host mesh fitting was used to transform the DTMRI fibre vectors into the geometric model-based on the in vivo tagged MRI data. The landmark points were the DTMRI surface contours segmented and defined in the cardiac coordinate system. The corresponding target points were the projections of the DTMRI surface contours onto the surface of the tagged model. The landmark points were embedded into a cuboid host mesh consisting of $2 \times 2 \times 2$ elements interpolated using tricubic Hermite basis functions. Then, the total squared distance between the embedded landmark points and target data points was minimized by adjusting the nodal parameters of the host mesh. This procedure ensured that the LV shape between tagged MRI and DTMRI was consistent. To transform the entire set of fibre locations within LV myocardium, they were also embedded in the undeformed host mesh and their locations and orientations were subjected to the same host mesh transformation. A transformation matrix was calculated for each fibre location, and the rotational component of each matrix was applied to the corresponding fibre vector in order to calculate its orientation in the reference model.

The fibre angle θ (defined as positive for an elevation angle above the short-axis plane) was calculated for each vector prior to fitting. It was assumed that fibre vectors lay parallel to the $\xi_1 - \xi_2$ plane, and imbrication angles and sheet angles were neglected in this study. The direct correspondence between the primary eigenvector and fibre direction has been well-

established (Scollan et al., 1998; Hsu et al., 1998). Myofibre orientations were incorporated into the geometric model as a fibre angle field (interpolated using tri-cubic Hermite basis functions), which was fitted using nonlinear optimisation. Fig. 8b and c illustrate the LV model with the fitted fibre orientation field and demonstrate the transmural variation throughout the LV wall.

4. Tag motion detection

After generating the anatomical FE model, the tag motion was extracted and used to tune the mechanics simulations. For the tissue tagging data, two separate sets of tag planes were created orthogonal to the image plane with a temporal resolution of 8 ms following the detection of the *R* wave of the ECG. Interactive image segmentation and tracking software developed by Young et al. (1995) was used to reconstruct regional LV deformation directly and simultaneously from both short-axis (12 slices, 60 frames) and long-axis (12 slices, 60 frames) images. The tracking process is summarised below.

1. Epicardial and endocardial contours were segmented for both short-axis (Fig. 9a) and long-axis (Fig. 9b) images with the aid of a guide-point model (Young et al., 2000) at each frame (60 frames per cardiac cycle).
2. A 16-element FE geometric model was created at each time frame based on the segmented contours from (1) using least squares optimisation.
3. A grid of tag lines covering the LV myocardium was overlaid onto the tagged images.
4. For each short-axis image at each time frame, horizontal and vertical tag lines were tracked sequentially. Fig. 9c and d illustrate the short-axis tracked horizontal tags at the end-diastolic (ED) frame and end-systolic (ES) frame, respectively. Fig. 9e and f shows the short-axis tracked vertical tags at the ED and ES frame, respectively.
5. The horizontal tag lines were tracked in the long-axis images at each frame.
6. Tag lines from both the short-axis and long-axis series were combined and tag motion within the myocardium was reconstructed in 3D using algorithms detailed in Young et al. (1995).

A set of 3D material points, which were embedded in the FE model, were created at the ED frame. The motions of the embedded material points in subsequent time frames were then derived. This provided in vivo material (Lagrangian) kinematic information of the LV motion, which was later used to tune the FE simulations.

5. Passive left ventricular mechanics

5.1. Finite deformation elasticity

Passive LV mechanics was simulated using the finite element method (FEM) to solve the stress equilibrium equations that govern finite deformation elasticity. We considered a two-state quasi-static analysis for this study: (1) the unloaded state (LV cavity pressure is zero) of

the material; (2) the deformed state due to pressure loading constraints. The finite deformations and traction field acting on the material are represented by strain (a measure of length change or displacement gradient) and stress (force per unit area on an infinitesimally small plane surface within the material). The equations governing large deformation mechanics were derived from the laws of conservation of mass, linear momentum, angular momentum and the principle of virtual work (Malvern, 1969). Key components and equations leading to the governing equations for finite deformation elasticity are summarised below.

The deformation gradient tensor (F) relates a material segment in the deformed state (\mathbf{x}) to the same material segment in the reference configuration (\mathbf{X}) (Eq. (3)).

$$F_M^i = \frac{\partial \chi_i}{\partial X_M} \quad (3)$$

The Lagrangian Green's strain tensor (E) is determined using (Eq. (4)).

$$E = \frac{1}{2}(F^T F - I) \quad (4)$$

where I is the identity matrix.

The second Piola–Kirchhoff stress tensor (T) represents the force measured per unit undeformed area over an element of surface in the undeformed configuration. Conservation of linear momentum equates the change of the total linear momentum over time to the vector sum of all the external forces acting on the material. In the absence of accelerations and body forces, this momentum balance reduces to the stress equilibrium equations in Eq. (5).

$$\frac{\partial}{\partial X_M} \left(T^{MN} \frac{\partial \chi_j}{\partial X_N} \right) = 0 \quad (5)$$

Conservation of angular momentum guarantees that the Cauchy and second Piola–Kirchhoff stress tensors are symmetric, by equating the change of the total angular momentum over time to the vector sum of the moments of the external forces acting on the system (Spencer, 1980). This reduces the number of independent stress tensor components from 9 to 6 (three normal components and three shear components). The principle of virtual work relates the surface traction s in static equilibrium with the internal stress vector, t when the body is subject to displacement δv . The second Piola–Kirchhoff stress tensor (T) can then be expressed as follows:

$$\int_V T^{MN} \frac{1}{J} \frac{\partial \chi_j}{\partial X_M} \frac{\partial \delta v_j}{\partial X_N} dV = \int_{S_2} s \cdot \delta v dS \quad (6)$$

The stress–strain relationship between stress components and deformation characterizes the mechanical function of individual materials. Eq. (7) expresses the second Piola–Kirchhoff stress tensor (T) in terms of the Lagrangian Green’s strain tensor (E) via the strain energy density function W (described below).

$$T^{MN} = \frac{1}{2} \left(\frac{\partial W}{\partial E_{MN}} + \frac{\partial W}{\partial E_{NM}} \right) - p \frac{\partial X_M}{\partial \chi_k} \frac{\partial X_N}{\partial \chi_k} \quad (7)$$

The variable p is a reaction stress (also known as the hydrostatic pressure) that arises due to the incompressible nature of the tissue. To provide continuous strain and stress distributions, a trilinear Lagrange interpolation scheme was chosen for the hydrostatic pressure.

The governing equations described above are assembled and solved using nonlinear Galerkin finite element techniques to determine the deformed state of the body under specified boundary conditions. These equations form a set of nonlinear residuals that can be solved using Newton’s method, which linearizes the equations. The resulting linear system can be solved using LU decomposition (Nash and Hunter, 2000). The initial solution for the finite elasticity equations is chosen to be the undeformed geometry modified by any kinematic constraints. Convergence of Newton’s method is highly dependent on the initial conditions and the non-linearity of the system, thus incremental load step are often required.

5.2. Loading constraints

The integrated model presented in this paper not only combined in vivo tagged MR data and ex vivo DTMRI data, but also incorporated in vivo LV cavity pressure recordings, which were temporally synchronized with the imaging data. Concurrent pressure recordings were achieved by inserting a MR compatible Miller transducer into the left ventricular cavity before tagged MRI data were acquired. Fig. 10 illustrates the synchronization of pressure recording with imaging trigger and right atrial pacing. There were three sets of pressure measurements corresponding to three data acquisitions: short-axis horizontal tagging, short-axis vertical tagging and long-axis horizontal tagging. The pressure trace obtained during short-axis vertical tag experiment was used for the mechanics simulations.

The passive diastolic filling phase was simulated by inflating the reference LV model to a pressure of 0.5 kPa to match the pressure recordings at the end-diastolic state. This load was applied to the endocardial surface of the model as a pressure boundary constraint in incremental steps of 0.1 kPa. We imposed kinematic constraints at the base and apex of the model. The long-axis (x) positions of the basal plane were prescribed to match the tag plane movements tracked from the long-axis images. At the apex of the model, the endocardial

and epicardial nodal parameters were fixed in the short-axis (y, z) plane during the simulations.

5.3. Constitutive relations

There have been numerous experiments and theoretic approaches to characterize the constitutive behaviour the heart, with particular attention being paid to the passive mechanical properties. Studying the material behaviour of myocardium is increasingly important because it serves not only as the bridge between stress field prediction and strain field measurement, but also as a potentially useful clinical indication of cardiac diseases (Abraham et al., 2006).

It is well-established that myocardium exhibits anisotropic, nonlinear, time-dependent and three dimensionally complex properties (Nash and Hunter, 2000; Costa et al., 2001). Experimental measurement of stress and strain (force–displacement) of trabeculae or papillary muscles was the first approach taken to investigate the properties of myocardium. Because the constitutive relations obtained from those preparations were restricted to one-dimension, conclusions drawn from these experiments are difficult to extend to more complex structures. Subsequently, bi-axial testing of tissue samples was performed (Fung, 1981). Although, the bi-axial test was able to capture more behavioural information and demonstrate anisotropy, it was difficult to discern the variations of stiffness in the fibre versus cross-fibre direction (Guccione et al., 1991). Whether or not the same findings can be found in intact heart still remains unsolved. After histological sectioning of ventricular tissue, LeGrice et al. (1995) revealed fibres organised as sheets that are tightly bound by endomyial collagen and loosely bound by perimysial collagen. This investigation raised a new set of local fibre coordinates defined by the fibre, sheet and sheet-normal directions. The sliding between adjacent sheets is a significant component of total LV wall thickening during systole (Costa et al., 1999). Based on these observations, Costa et al. (2001) developed an experimental constitutive relation to represent orthotropic mechanical behaviour, which Schmid et al. (2006) used to fit parameters to in vitro samples of pig ventricular myocardium. Although recent research by Helm et al. (2006) reported correlations between the tertiary eigenvectors derived from DTMRI and sheet-normal direction, more investigations are required to verify the orthotropic fibre structure derived from DTMRI. Therefore in the present study, we only have access to fibre orientation data from ex vivo DTMRI for this model. Consequently the stress–strain behaviour of the ventricular myocardium in this study was modelled using the transversely-isotropic constitutive relation (exponential energy function) in Eq. (8) (Guccione et al., 1991).

$$W = C_1 \exp(Q) \quad (8)$$

$$\text{where } Q = C_2 E_{ff}^2 + C_3 (E_{cc}^2 + E_{rr}^2 + 2E_{cr}^2) + 2C_4 (E_{fc}E_{cf} + E_{fr}E_{rf})$$

where $E_{\alpha\beta}$ are the components of Green's (Lagrange) strain tensor referred to fibre (f), cross-fibre (c) and radial (r) material coordinates. $C_1 - C_4$ are the myocardial constitutive parameters. Based on experiments using isolated canine hearts, Omens et al. (1993)

estimated these parameters as 1.2 kPa, 26.7, 2.0, 14.7, respectively. We used these values as initial estimates during our parameter identification procedure.

5.4. Constitutive parameter estimation

Material parameter estimation was implemented in CMISS using the sequential quadratic programming (SQP) optimisation technique, which is sometimes considered as an extension of Newton and quasi-Newton methods for constrained optimisation problems (Boggs and Tolle, 1995). SQP iteratively finds a better approximation to a nonlinear problem using quadratic programming of a sub-problem with a given approximation. The parameters were tuned by matching model predictions to the set of 3D material points derived from MRI tagging, as described in Section 4. The sum of squared Euclidean distances between the predicted positions and in vivo tracked positions of these material points formed the objective function. This algorithm is illustrated in Fig. 11.

Augenstein et al. (2005) and Omens et al. (1993) reported coupling between the material coefficients in the exponential term of the transversely-isotropic material relation. We therefore designed a sequential optimisation algorithm to evaluate these parameters. After first optimising C_1 , we sequentially optimised C_2 , C_3 and C_4 independently, and repeated this until these parameters and the RMSE converged.

6. Results

The optimal value of C_1 , C_2 , C_3 and C_4 were found to be 0.831 kPa, 14.31, 4.49 and 0.762, (see Table 1). The use of these parameters in the model also provided a good match between the FE predicted end-diastolic LV cavity volume with that derived from the tagged MR images (both estimates were 23 ml). Table 2 shows the comparison of estimated parameters from this study with Omens et al. (1993) and Augenstein et al. (2005). In our hands, the estimated value for C_4 was small compared with values obtained from the other two studies. Given the importance of shear modes in myocardial deformation (Schmid et al., 2008; LeGrice et al., 1995), we speculate that this parameter may not be identifiable based on the typical diastolic deformations.

Using the estimated material parameters, we calculated the maximum principle strain at a set of embedded material points derived from tagged MR images. As Fig. 12 indicates, the largest strains occurred around the most basal region of the model.

The stress tensor was evaluated using the local strain and the optimised constitutive parameters at the optimum. The spatial distribution of maximum principal stress is illustrated in Fig. 13. Stress was maximal at the endocardial surface around basal region where the endocardial pressure loading was applied and maximum displacements occurred.

7. Discussion

The primary objective of this study was to estimate the in vivo passive material properties of myocardium using a finite element LV model that integrates accurate in vivo geometry, ex vivo myofibre orientations, and in vivo loading conditions. Simulation of the diastolic LV

mechanics using this model and subsequent comparison against observed regional deformations derived from cine tagged MR images allowed us to estimate the passive constitutive parameters of the LV. We have developed a FE based modelling method to integrate cardiac structural and functional measurements derived from in vivo canine tagged MRI, LV cavity pressure data, and ex vivo DTMRI microstructural information from the same heart. The high spatial and temporal resolution of this tagged MRI data set allowed us to describe the LV kinematics during diastolic filling, and the tag resolution provided the ability to quantify all components of the three-dimensional Lagrangian strain, including regional radial strain, which for the first time could be used for parameter estimation. In this paper, although the finite element prediction of the left ventricular wall motion we presented is seemingly similar to motion recovery, our technique is based on nonlinear finite elastic deformation of a computational model, designed to be physiologically realistic. This is different to inverse problem using meshfree state-space framework (Wong et al., 2006, 2009) or motion recovery using image force (Billet et al., 2009). We aim to combine the two most advanced cardiac mechanics imaging tools (tagged MRI and diffusion tensor MRI) to provide us with accurate and realistic heart geometry and fibre architecture to study regional mechanical function of the heart (such as the myocardial stress, strain, and stiffness distributions) and this is only plausible with the aid of finite element modelling. Compared to the existing image-processing based methods, our proposed framework relies less on the image processing and makes a good candidate for 3D motion analysis, regional strain and stress analysis as well as parameter estimation. However, direct comparison of motion results between our study and recent works on motion recovery can be challenge.

7.1. Mapping DTMRI data to tagged MR model

Currently, DTMRI cannot provide reliable in vivo data due to image artifacts arising from the motion of the beating heart that can confound quantitative measures of myofibre orientation. Thus, the technique is presently limited to ex vivo studies. When the heart is excised, it is fixed in a quasi-end-diastolic state and therefore differs in shape when compared to the in vivo tagged MRI heart shape. There have been several attempts to combine cardiac MRI functional data with DTMRI into a computational model for finite element analysis of ventricular mechanics (Augenstein et al., 2005; Sermesant et al., 2006a,b; Walker et al., 2004, 2008). The use of the affine transformation along with image feature alignments is a common bulk registration method for combining tagged MRI data with DTMRI data (Walker et al., 2004; Sermesant et al., 2006a). Such techniques involve: (1) least-squares alignment of the geometry from the two data sets; or (2) least-squares alignment of the valve plane, LV long-axis and right-ventricular insertion points (Walker et al., 2004). These methods align the gross geometry of the LV in the two images sets, but do not account for regional transformations nor the transformation of the ex vivo fibre direction to the in vivo geometry. The free form deformation method that we have developed in this study registers the LV geometry and maps the fibre orientations from the ex vivo to the in vivo geometric configuration on a localised basis.

7.2. Material parameter estimation

Previous work on estimating in vivo material properties from MRI has focused primarily on the following aspects: (1) using a statistical-model approach to quantify the stress and strain

distribution and in vivo material properties based on motion provided by non-invasive tagged MRI (Hu et al., 2003); (2) investigating the regional elastic moduli using MRI-based techniques, such as displacement-encoding with stimulated-echoes (DENSE) and phase-contrast (PC) velocity mapping (Wen et al., 2005); (3) establishing a full electro-mechanical model (based on small-strain, linear elasticity theory) from 3D-images of the heart to simulate ventricular mechanics (Sermesant et al., 2006a,b); (4) using MRI-based finite element analysis to estimate parameters of a transversely-isotropic material relation based on in-plane strains (Walker et al., 2008). This latter study is the most similar to the present study, however, increased spatial resolution now allows direct comparison of transmural strains. Furthermore, greater temporal resolution allows us to more reliably identify the precise timing of end-diastole.

There are marked differences between the parameters estimated in this study and those obtained by Omens et al. (1993) and Augenstein et al. (2005) (see Table 2). This may reflect differences in the myocardial muscle properties between the different hearts used during the experiments; it may be due to the different modelling assumptions (such as the application of different loading constraints) or different experimental conditions (in vivo versus in vitro); it may even arise from the non-uniqueness of the parameter identification process. Moreover, these parameters were only derived from one set of canine data.

Parameter estimation can be sensitive to a number of factors such as: noise level in the MRI data; the number of image frames introduced in the optimisation, (Augenstein et al., 2005), and the assumed loading and kinematic constraints. The effects of altering noise level in the tagged MR data and number of image frames were investigated by Augenstein et al. (2005) using Monte Carlo simulation. They concluded that more image frames needed to be included in the optimisation as they increased the noise in the tagged MRI data.

The present estimation strategy is based on two states of the LV: reference (unloaded) and end-diastolic state (loaded). As proposed by Augenstein et al. (2005), we could also take advantage of the image frames between the two states as intermediate steps. The concurrent pressure recordings will be useful in this approach. We also tracked material points' displacements at all frames during the cardiac cycle, hence FE simulated results after each image frame can be validated. This approach should allow us to incorporate more detailed LV motion into the optimisation, thereby providing a better estimate of the passive material parameters. However, the computational expenses of this approach needs addressing.

7.3. Boundary conditions

Appropriate boundary conditions and loading constraints are also essential for modelling myocardial mechanics. The epicardium and endocardium as well as base and apex experience different displacements and loads. Kinematic constraints are typically used to fix basal movement (or at least certain components of the base), but to allow the apex to move freely (Remme et al., 2004; Walker et al., 2008). We extracted displacement boundary conditions for the basal plane from the tagged long-axis and short-axis images. From our observation, the apex of the heart did not move significantly during diastole, as opposed to the mitral valve plane. Therefore, we prescribed the displacement for the nodes at the basal plane to ensure a physiologically realistic deformation was simulated.

7.4. Limitations

For the DTMRI and tagged MRI registration, one limitation of the host mesh fitting technique is that we only used the surface boundaries of the FE model and DTMRI of the LV to calculate the transformation from the in vivo state to the ex vivo state. An improved approach would use a scaled response of the displacement field extracted from the tagged MRI images to define the correspondence of the geometry and fibre directions, thereby potentially improving the intramural correspondence.

The loading and kinematic constraints play important roles in determining myocardium mechanical behaviour. During inflation, we applied the observed pressure uniformly over the endocardial surface. However, this may not be appropriate, because we are neglecting the inertia of the blood when it enters the LV. One solution might be to apply a pressure gradient to the endocardial surface, but further data regarding this type of variation must be identified. The basal plane constraints may be relaxed when an appropriate pressure gradient is present inside of the LV cavity.

Another limitation of our model was lack of a right ventricle (RV), which is known to contribute to the kinematic and loading constraints at the septum. Hence, the effect of the RV on LV motion is not incorporated in the mechanics simulation. The presence of the RV would likely alter the material parameter estimation for the LV. However, this model can be extended to contain both ventricles.

The RMS error (~1.81 mm) between the predicted and tracked material points is marked in some regions. Consideration of the motion of the tracked points indicates that the basal region moved upwards (away from the apex) whereas the points around the apical region moved away from the base. Our current model was not able to fully reconstruct this motion. It is possible that using a heterogeneous distribution of material parameters may be necessary. Furthermore, the present model has not yet included imbrication angles and sheet angles, which may be a further source of error given the known occurrence of these microstructural features.

8. Conclusions

We have established a FE model-based technique to estimate in vivo material parameters with accurate geometric, kinematic and microstructural information of the LV. We successfully simulated passive inflation and customized material parameters of a transversely-isotropic material relation by matching observed kinematic information derived from the tagged MRI. The high tag resolution offered by this MRI data provides us with localised 3D strain measurements, which we can use to estimate constitutive parameters. This type of modelling may be used to provide us with insight into regional distributions of myocardial stress and functional measures such as local energy consumption. Comparing models of healthy and diseased states will also allow us to investigate the underlying mechanisms for LV dysfunction.

Acknowledgements

The authors gratefully acknowledge financial support from the Health Research Council (HRC) of New Zealand. V. Wang is supported by the New Zealand Institute of Mathematics and its Applications (NZIMA). M. Nash is supported by a James Cook Fellowship administered by the Royal Society of New Zealand on behalf of the New Zealand Government. We would like to acknowledge Professor Elliot McVeigh from National Institutes of Health and Johns Hopkins University for providing the experimental data.

References

- Abraham TP, Lardo AC, Kass DA, 2006 Myocardial dyssynchrony and resynchronization. *Heart Fail Clin* 2, 179–192. [PubMed: 17386888]
- Augenstein KF, Cowan BR, LeGrice IJ, Nielsen PM, Young AA, 2005 Method and apparatus for soft tissue material parameter estimation using tissue tagged magnetic resonance imaging. *J. Biomech. Eng* 127, 148–157. [PubMed: 15868797]
- Axel L, Dougherty L, 1989 Heart wall motion: improved method of spatial modulation of magnetization for MR imaging. *Radiology* 172, 349–350. [PubMed: 2748813]
- Billet F, Sermesant M, Delingette H, Ayache N, 2009 Cardiac motion recovery and boundary conditions estimation by coupling an electromechanical model and cine-MRI data *Functional Imaging and Modeling of the Heart*, Springer, Berlin/Heidelberg pp. 376–385.
- Boggs PT, Tolle JW, 1995 Sequential quadratic programming. *Acta Numer* 4, 1–51.
- Bradley CP, Pullan AJ, Hunter PJ, 1997 Geometric modeling of the human torso using cubic hermite elements. *Ann. Biomed. Eng* 25, 96–111. [PubMed: 9124743]
- Costa KD, Takayama Y, McCulloch AD, Covell JW, 1999 Lamina fiber architecture and three-dimensional systolic mechanics in canine ventricular myocardium. *Am. J. Physiol. Heart. Circ. Physiol* 276, H596–H607.
- Costa KD, Holmes JW, McCulloch AD, 2001 Modelling cardiac mechanical properties in three dimensions. *Phil. Trans. Royal Soc. London*, 1233–1250.
- Demer LL, Yin FC, 1983 Passive biaxial mechanical properties of isolated canine myocardium. *J. Physiol* 339, 615–630. [PubMed: 6887039]
- Ennis DB, 2004 Assessment of Myocardial Structure and Function Using Magnetic Resonance Imaging Ph.D. Thesis John Hopkins University.
- Ennis DB, Nguyen TC, Riboh JC, Wigström L, Harrington KB, Daughters GT, Ingels NB, Miller DC, 2008 Myofiber angle distributions in the ovine left ventricle do not conform to computationally optimized predictions. *J. Biomech* 41, 3219–3324. [PubMed: 18805536]
- Fung YC, 1981 *Biomechanics: Mechanical Properties of Living Tissues* Springer-Verlag, New York.
- Glass L, Hunter P, McCulloch AD (Eds.), 1991 *Theory of Heart: Biomechanics, Biophysics and Nonlinear Dynamics of Cardiac Function* Springer, New York.
- Guccione JM, McCulloch AD, Waldman LK, 1991 Passive material properties of intact ventricular myocardium determined from a cylindrical model. *J. Biomech. Eng* 113, 43–55.
- Helm PA, Beg MF, Miller MI, Winslow RL, 2005 Measuring and mapping cardiac fiber and lamina architecture using diffusion tensor MR imaging. *Ann. NY Acad. Sci* 1047, 296–307. [PubMed: 16093505]
- Helm PA, Younes L, Beg MF, Ennis DB, Leclercg C, Faris OP, McVeigh E, Kass D, Miller MI, Winslow RL, 2006 Evidence of structural remodeling in the dyssynchronous failing heart. *Circ. Res* 98, 125–132. [PubMed: 16339482]
- Hsu EW, Muzikant AL, Matulevicius SA, Penland RC, Henriquez CS, 1998 Magnetic resonance myocardial fiber-orientation mapping with direct histological correlation. *Am. J. Physiol* 275, H1627–H1634. [PubMed: 9815070]
- Hu Z, Metaxas D, Axel L, 2003 In vivo strain and stress estimation of the heart left and right ventricles from MRI images. *Med. Image Anal* 7, 435–444. [PubMed: 14561549]
- LeGrice IJ, Smaill BH, Chai LZ, Edgar SG, Gavin JB, Hunter PJ, 1995 Lamina structure of the heart: ventricular myocyte arrangement and connective tissue architecture in the dog. *Am. J. Physiol. Heart Circ. Physiol* 269, H571–H582.

- Malvern LE, 1969 Introduction to the Mechanics of a Continuous Medium Prentice-Hall Inc, Englewood Cliffs, New Jersey.
- Maron BJ, Anan TJ, Roberts WC, 1981 Quantitative analysis of cardiac muscle cell disorganization in the left ventricular wall of patients with hypertrophic cardiomyopathy. *Circulation* 63, 882–894. [PubMed: 7193536]
- Nash MP, Hunter PJ, 2000 Computational mechanics of the heart. *J. Elast* 61, 113–141.
- Nielsen PMF, 1987 The Anatomy of the Heart: A Finite Element Model Ph.D. Thesis University of Auckland.
- Omens JH, MacKenna DA, McCulloch AD, 1993 Measurement of strain and analysis of stress in resting rat left ventricular myocardium. *J. Biomech* 26, 665–676. [PubMed: 8514812]
- Remme EW, Hunter PJ, Smiseth O, Stevens C, Rabben SI, Skulstad H, Angelsen B, 2004 Development of an in vivo method for determining material properties of passive myocardium. *J. Biomech* 37, 669–678. [PubMed: 15046996]
- Schmid H, Nash MP, Young AA, Hunter PJ, 2006 Myocardial material parameters estimation – a comparative study for simple shear. *J. Biomech. Eng* 128, 742–751. [PubMed: 16995761]
- Schmid H, O’Callaghan P, Nash MP, Lin W, LeGrice IJ, Smaill BH, Young AA, Hunter PJ, 2008 Myocardial material parameter estimation – a nonhomogeneous finite element study from simple shear tests. *Biomech. Model. Mechanobiol* 7, 161–173. [PubMed: 17487519]
- Scollan DF, Holmes A, Winslow R, Forder J, 1998 Histological validation of myocardial microstructure obtained from diffusion tensor magnetic resonance imaging. *Am. J. Physiol* 275 (6 Pt 2), H2308–H2318. [PubMed: 9843833]
- Sermesant M, Delingette H, Ayache N, 2006a An electromechanical model of the heart for image analysis and simulation. *IEEE Trans. Med. Imaging* 25, 612–625. [PubMed: 16689265]
- Sermesant M, Moireau P, Camara O, Sainte-Marie J, Andriantsimiavona R, Cimrman R, Hill DLG, Chapelle D, Razavi R, 2006b Cardiac function estimation from MRI using a heart model and data assimilation: advances and difficulties. *Med. Image Anal* 10, 642–656. [PubMed: 16765630]
- Spencer AJM, 1980 Continuum Mechanics. Longman Group Limited, London.
- Streeter DD, Spotnitz HM, Patel DP, Ross J, Sonnenblick EH, 1969 Fiber orientation in the canine left ventricle during diastole and systole. *Circ. Res* 3, 339–347.
- Ubbink S, Bovendeerd P, Delhaas T, Arts T, Van de Vosse F, 2006 Towards model-based analysis of cardiac MR tagging data: relation between left ventricular shear strain and myofiber orientation. *Med. Image Anal* 10, 632–641. [PubMed: 16723270]
- Walker JC, Ratcliffe MB, Zhang P, Wallace AW, Edward BF, Hsu W, Saloner D, Guccione JM, 2004 Magnetic resonance imaging-based finite element stress analysis after linear repair of left ventricular aneurysm. *Am. J. Physiol. Heart Circ. Physiol* 289, H692–H700.
- Walker JC, Ratcliffe MB, Zhang P, Wallace AW, Hsu EW, Saloner DA, Guccione JM, 2008 Magnetic resonance imaging-based finite element stress analysis after linear repair of left ventricular aneurysm. *J. Thorac. Cardiovasc. Surg* 135, 1094–1102. [PubMed: 18455590]
- Wang J, Nagueh SF, 2009 Current perspectives on cardiac function in patients with diastolic heart failure. *Circulation* 119, 1146–1157. [PubMed: 19255354]
- Wang VY, Lam HI, Ennis DB, Young AA, Nash MP, 2008 Passive Ventricular Mechanics Modelling Using MRI of Structure and Function, Medical Image Computing and Computer-assisted Intervention – MICCAI Springer, Berlin/ Heidelberg pp. 814–821.
- Wen H, Bennett E, Epstein N, Plehn J, 2005 Magnetic resonance imaging assessment of myocardial elastic modulus and viscosity using displacement imaging and phase-contrast velocity mapping. *Magn. Reson. Med* 54, 538–548. [PubMed: 16086299]
- Wong KCL, Zhang H, Liu H, Shi P, 2006 Physiome Model Based State-Space Framework for Cardiac Kinematics Recovery Springer, Berlin/Heidelberg.
- Wong KCL, Wang L, Shi P, 2009 Active Model with Orthotropic Hyperelastic Material for Cardiac Image Analysis, Functional Imaging and Modeling of the Heart Springer, Berlin/Heidelberg pp. 229–238.
- Young AA, Kraitchman DL, Dougherty L, Axel L, 1995 Tracking and finite element analysis of stripe deformation in magnetic resonance tagging. *IEEE Trans. Med. Imaging* 14, 413–421. [PubMed: 18215845]

- Young AA, Cowan BR, Thrupp S, Hedley W, Dell'Italia LJ, 2000 Left ventricular mass and volume: fast calculation with guide-point modelling on MR images. *Radiology* 216, 596–602.
- Zerhouni EA, Parish DM, Rogers WJ, Yang A, Shapiro EP, 1988 Human heart: tagging with MR imaging – a method for noninvasive assessment of myocardial motion. *Radiology* 169, 59–63. [PubMed: 3420283]

Author Manuscript

Author Manuscript

Author Manuscript

Author Manuscript

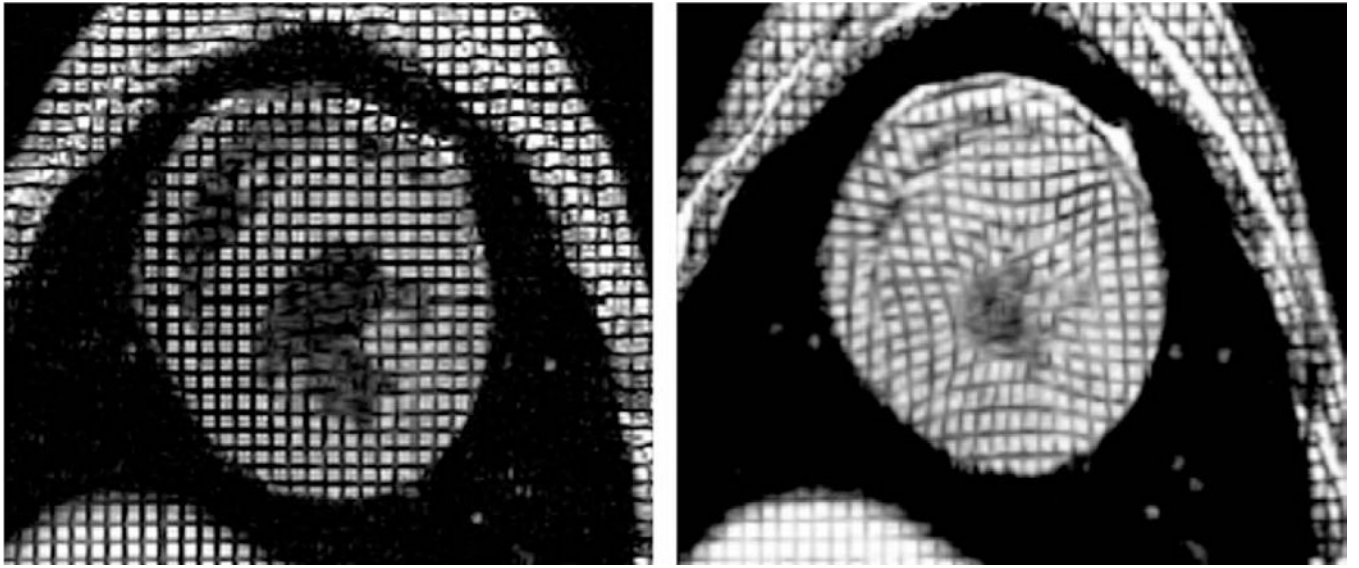


Fig. 1.
Short-axis tagged MR image of a beagle heart at end-diastole (left) and end-systole (right).

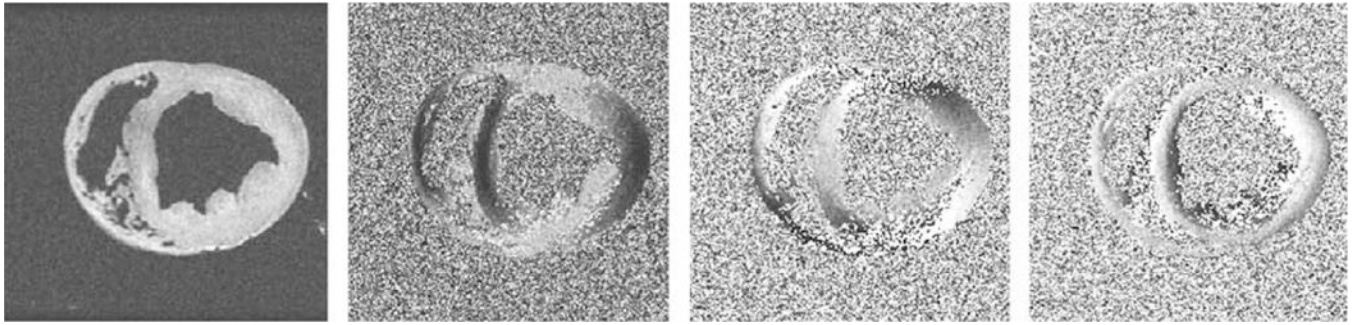


Fig. 2.
(Left to right) Anatomical ($b = 0$) image, and maps of x , y , and z components of the maximum diffusion eigenvector.

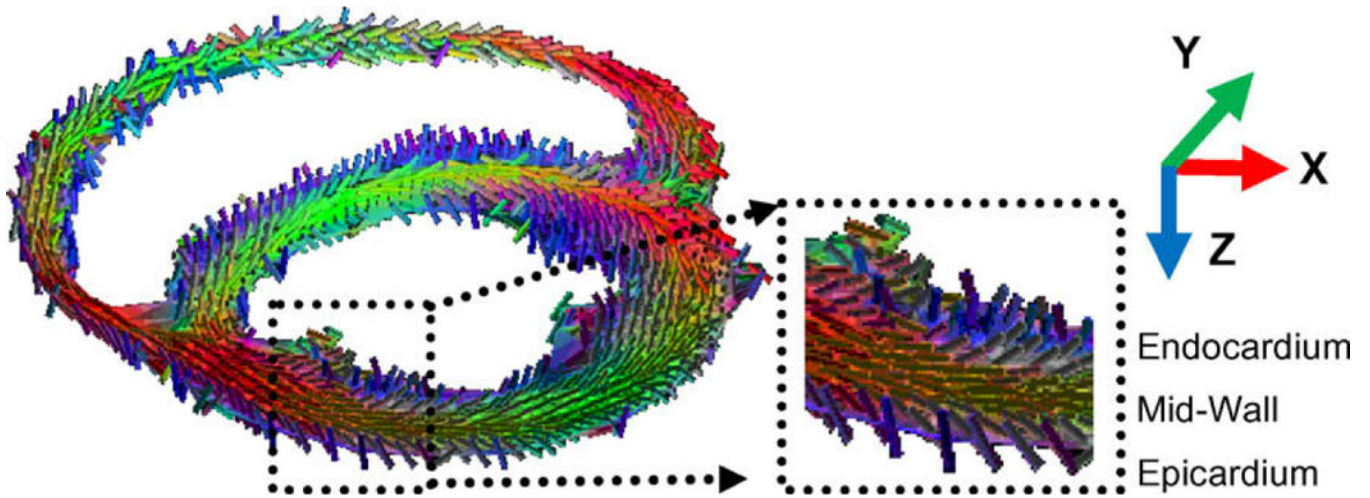


Fig. 3. 3D rendering of the maximum principal eigenvectors extracted from a mid-ventricular DTMRI slice. The colouring scheme is based on the global image coordinate system. For example, fibre vectors lying parallel to the x axis are colour-coded in red, vectors parallel to the y axis are green, and those orientated orthogonal to the x - y plane (vertically) are blue. (For interpretation of the references to colour in this figure legend, the reader is referred to the web version of this article.)

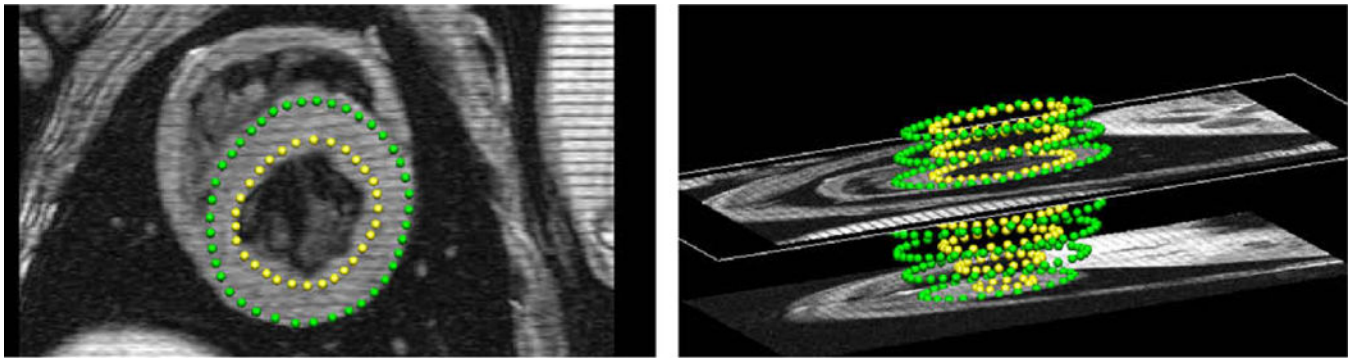


Fig. 4. Segmented contours on short-axis MR images in 2D and 3D views (yellow: endocardial surface contour, green: epicardial surface contour). (For interpretation of the references to colour in this figure legend, the reader is referred to the web version of this article.)

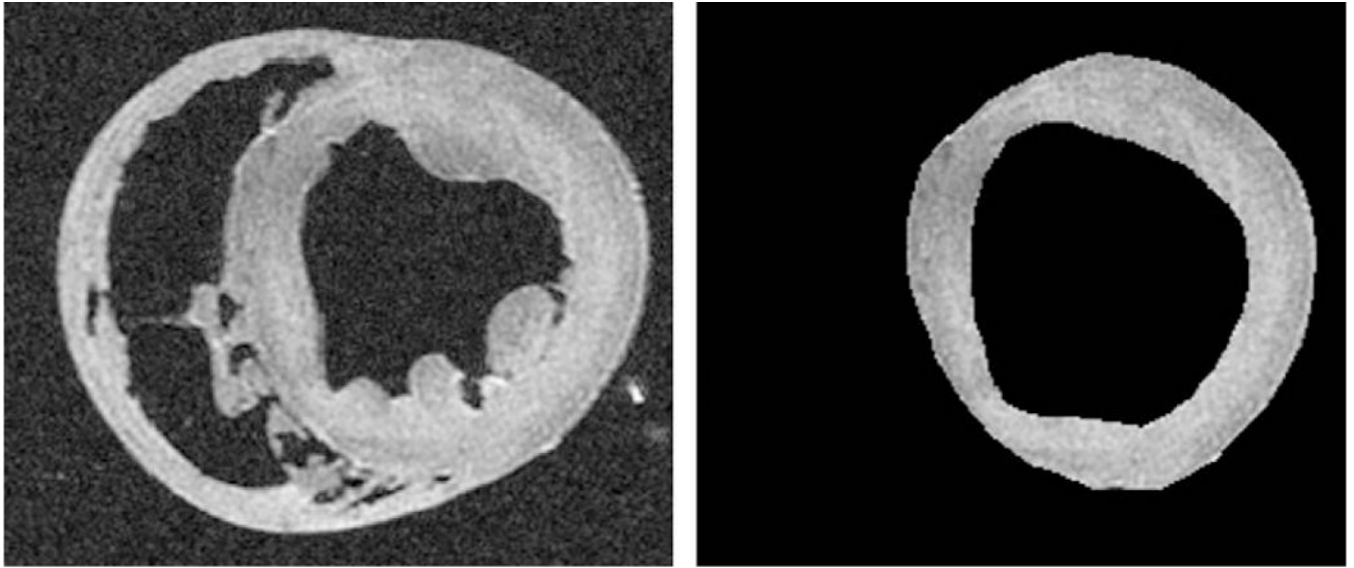


Fig. 5. Short-axis DTMR image (left) and masked LV myocardium on the same DTMR image (right).

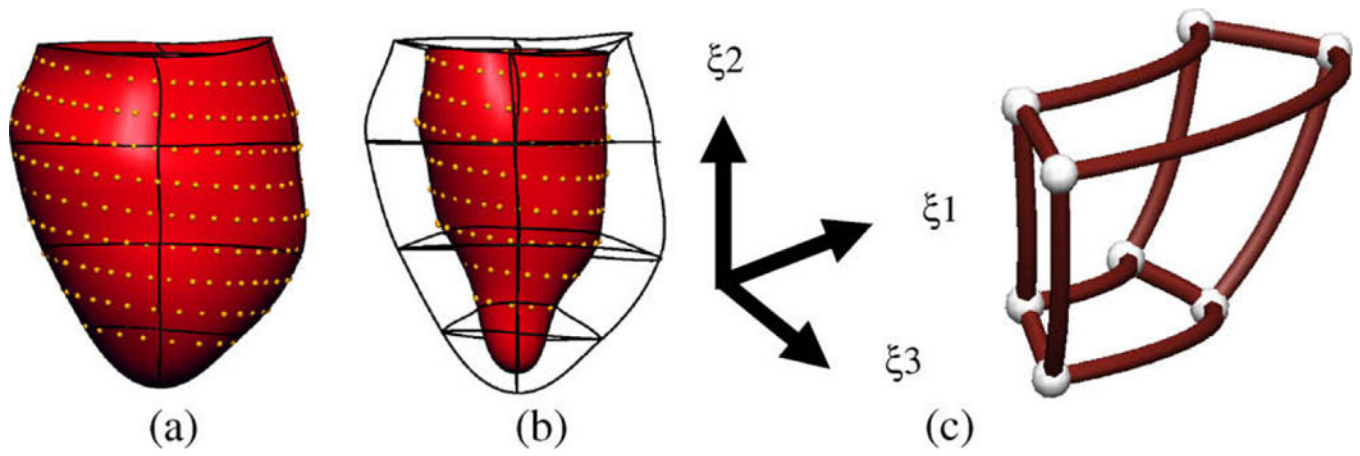


Fig. 6.

(a) Epicardial surface of a regular ellipsoid fitted to the segmented epicardial surface contours (RMSE = 0.33 mm); (b) endocardial surface of the model from (a) fitted to the segmented endocardial surface contour (RMSE = 0.31 mm); (c) a single finite element indicating the local material coordinate system.

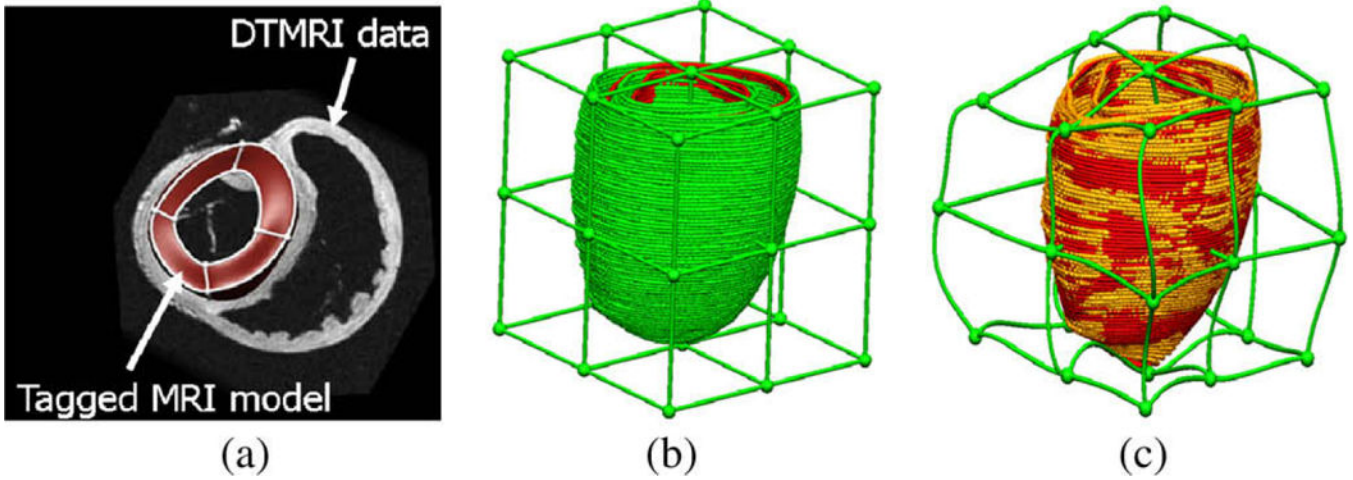


Fig. 7.

(a) Finite element geometric model overlaid with one short-axis DTMRI showing the misalignment between the two data sets. (b) Undeformed host mesh with landmark points (green) and target points (red); RMSE = 2.67 mm. (c) Deformed host mesh with updated landmark points (gold) and target points (red); RMSE = 0.47 mm. (For interpretation of the references to colour in this figure legend, the reader is referred to the web version of this article.)

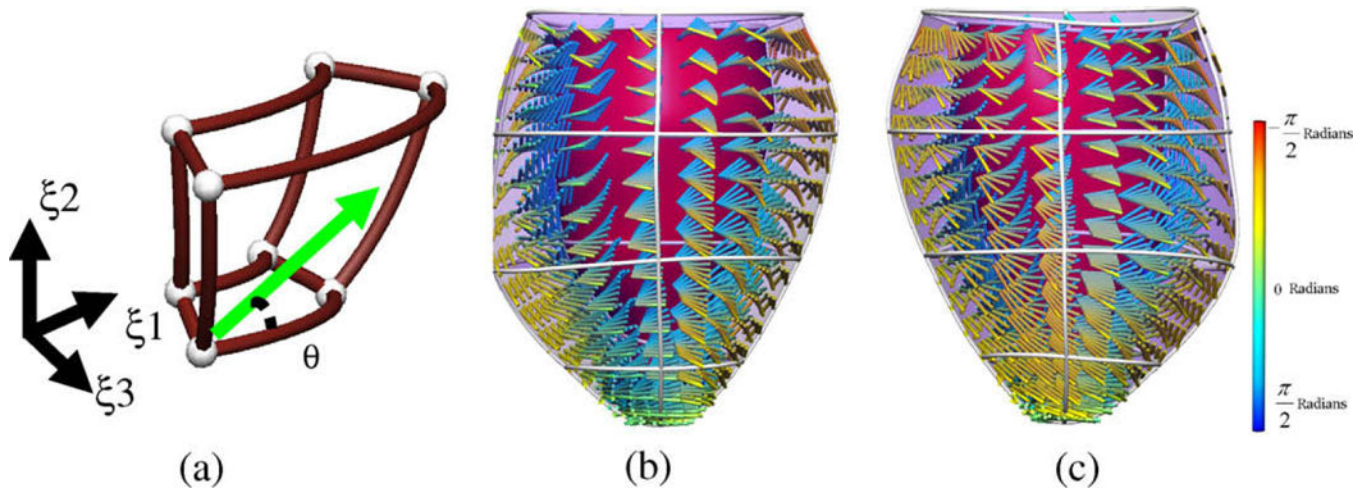


Fig. 8. Fibre orientation field defined as the elevation angle θ with respect to the short-axis plane (a). Anterior (b) and posterior (c) views of the LV model superimposed with the fitted fibre field.

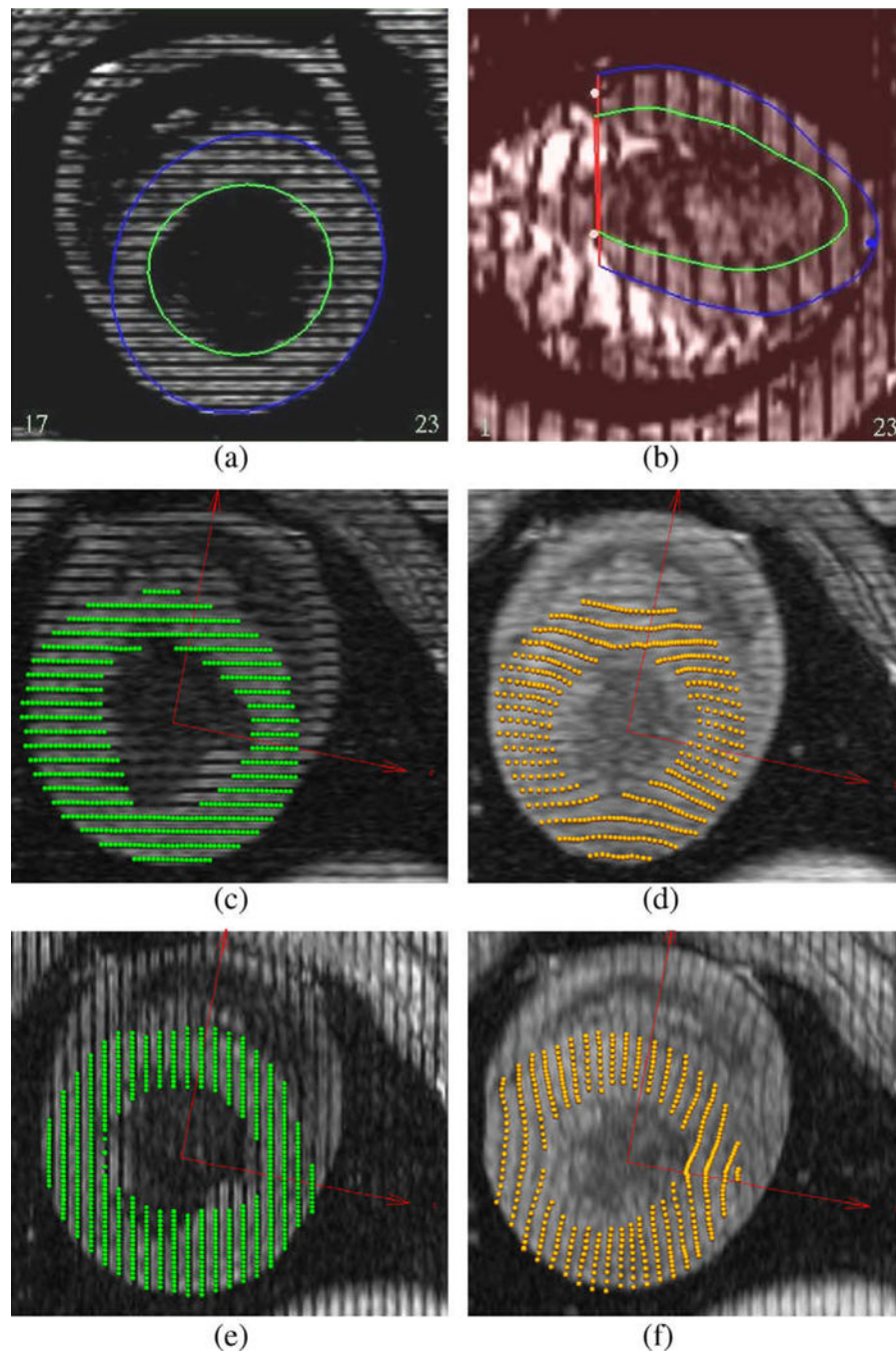


Fig. 9. Snapshot of segmented surface contours using a guide-point model for a mid-ventricular short-axis image (a) and a long-axis image (b); Tracked horizontal tags at the end-diastolic (ED) (c) and end-systolic (ES) (d) frames; Tracked vertical tags at the ED (e) and ES (f) frames.

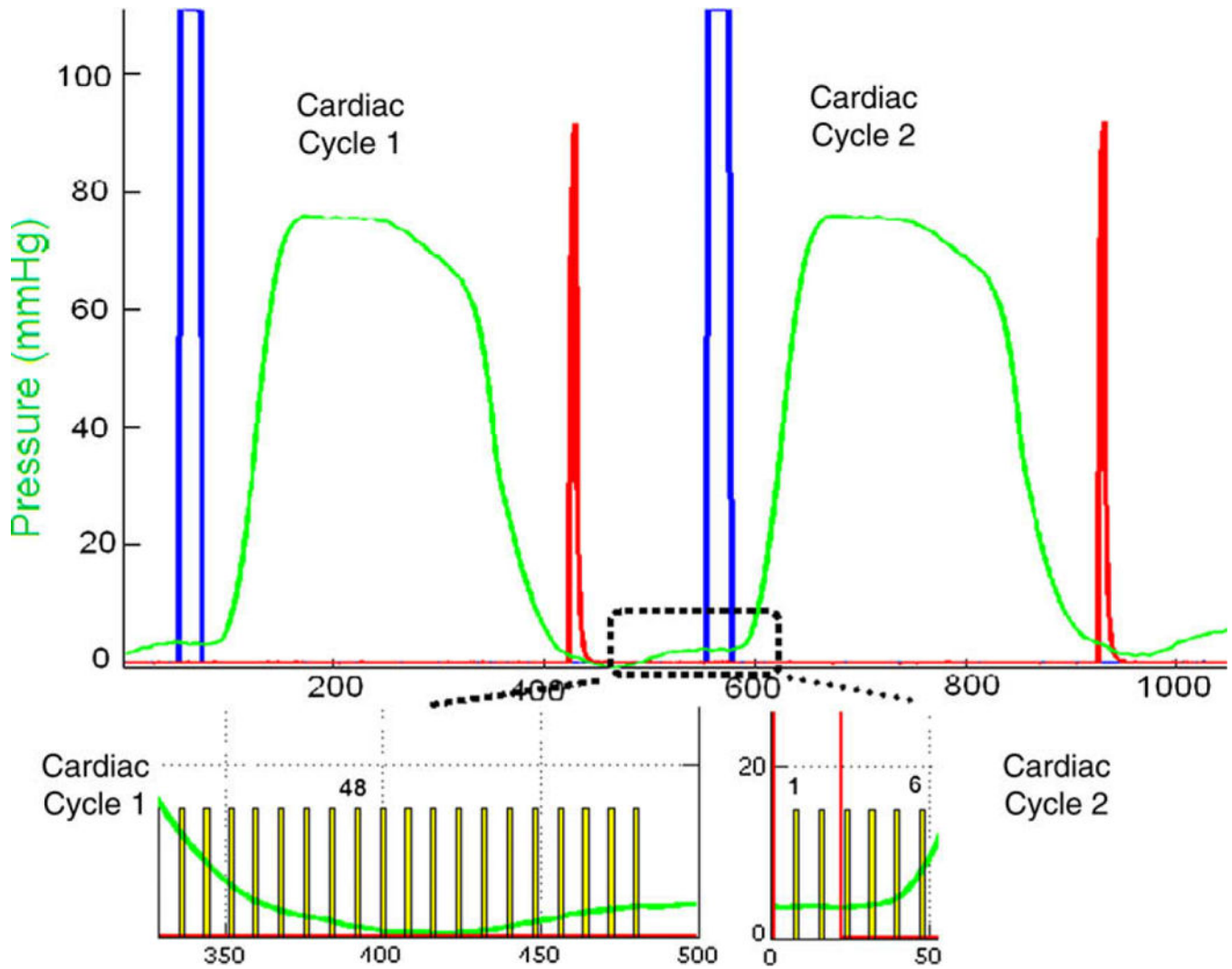


Fig. 10.

(Above) LV cavity pressure recording (green) overlaid with imaging trigger (blue) and right atrial pacing trigger (red) for two cardiac cycles. (Below) Pressure trace overlaid with spikes (yellow) indicating individual image frames from the start of diastolic inflation (frame 48) in cardiac cycle 1 to the end of diastole (frame 6) in cardiac cycle 2. Phases were determined based on observed valve function (see text for details). (For interpretation of the references to colour in this figure legend, the reader is referred to the web version of this article.)

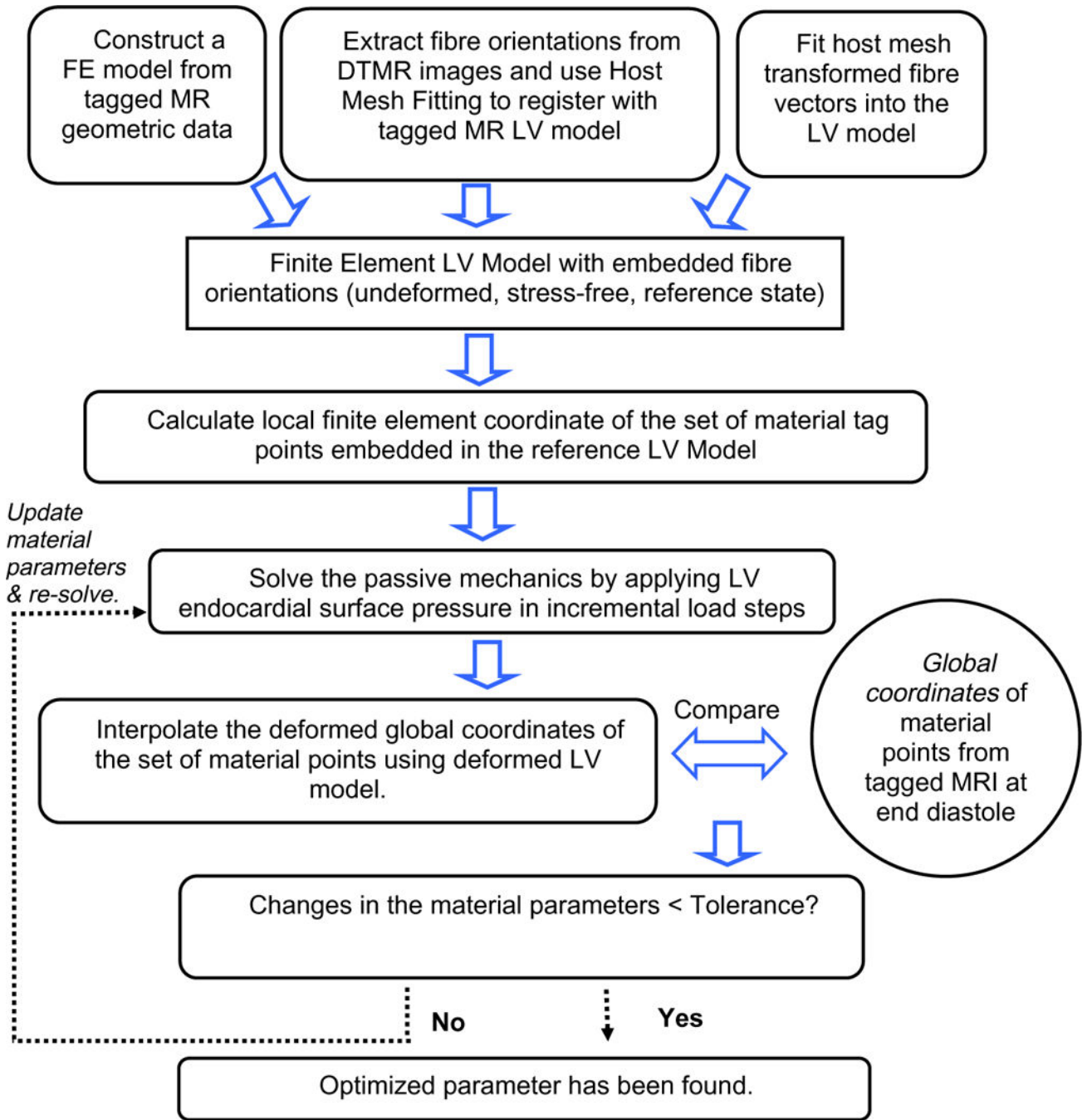


Fig. 11. Constitutive parameter estimation algorithm.

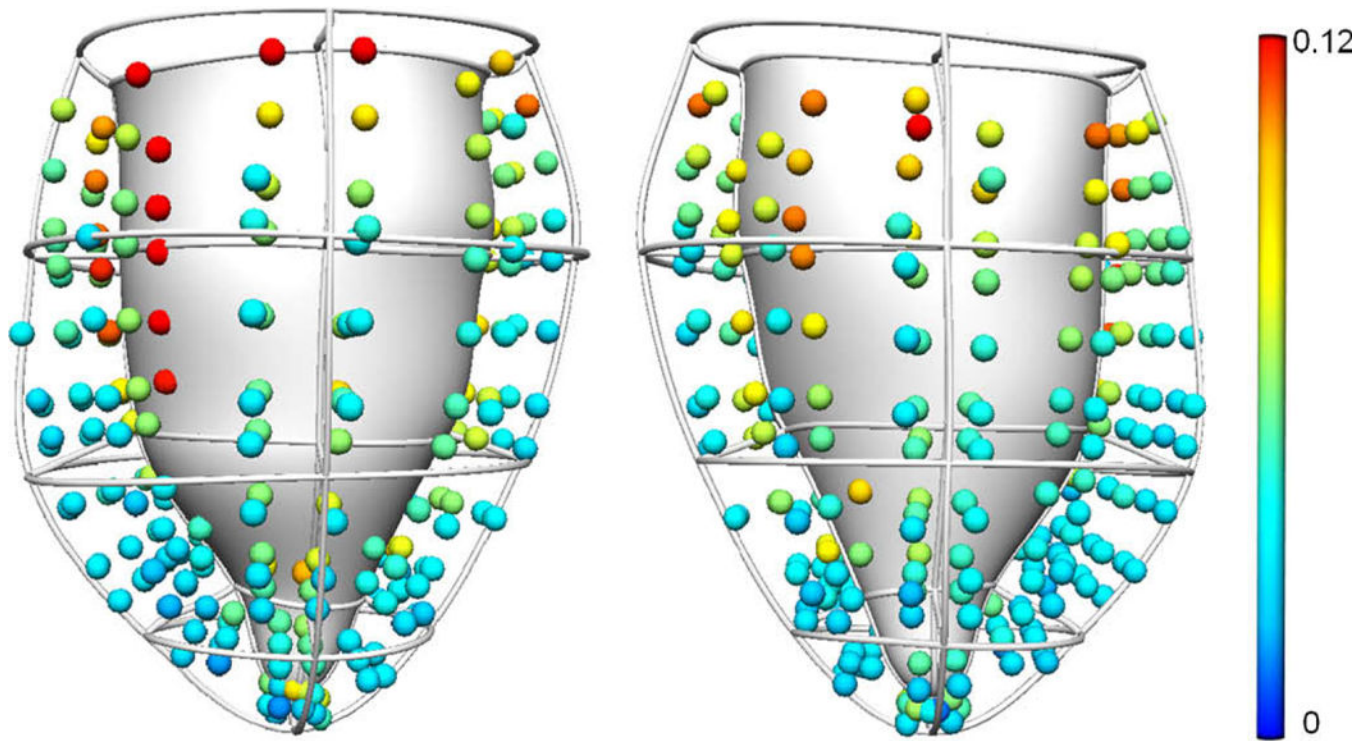


Fig. 12. (Left) Anterior and (right) posterior views of the maximum principal strain evaluated at material points derived from tagged MRI.

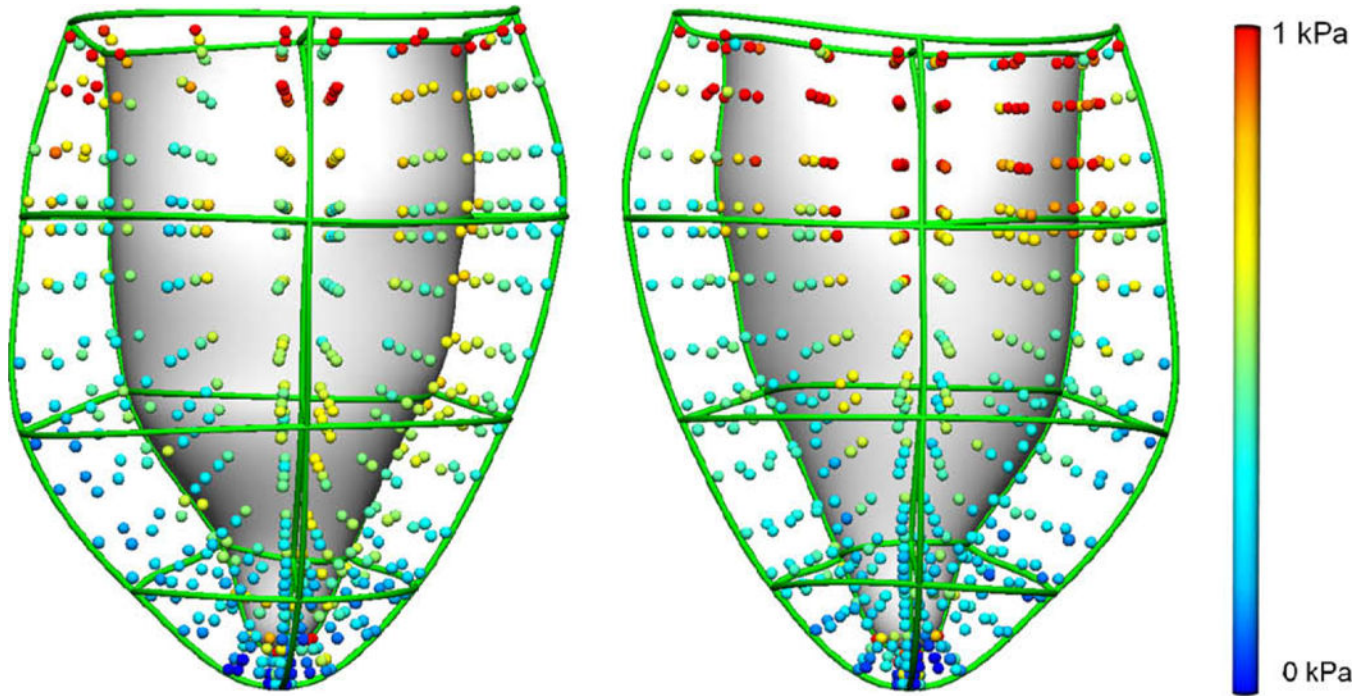


Fig. 13. (Left) Anterior and (right) posterior view of the maximum principal stress distribution at each Gauss point of the predicted end-diastolic model.

Constitutive parameter estimation. Values in boxes indicate the parameter being estimated during each optimisation.

Table 1

Optimisation number	C_1 (kPa)	C_2	C_3	C_4	Sum of squared differences (mm ²)	RMSD (mm) ^a
0	1.2	26.7	2.0	14.7	14742	2.24
1	0.831	26.7	2.0	14.7	13687	2.16
2	0.831	18.2	2.0	14.7	13342	2.13
3	0.831	18.2	4.26	14.7	11604	1.99
4	0.831	18.2	4.26	0.904	9875	1.84
5	0.831	16.10	4.26	0.904	9796	1.83
6	0.831	16.10	4.44	0.904	9788	1.82
7	0.831	16.10	4.44	0.762	9705	1.82
8	0.831	14.31	4.44	0.762	9638	1.81
9	0.831	14.31	4.49	0.762	9637	1.81

^aRMSD: root mean squared difference between material points' locations predicted from the model and those determined from tagged MRI

Table 2

Comparison of passive material parameters for canine hearts based on the transversely-isotropic exponential constitutive relation (Eq. (8)).

Studies	C_1 (kPa)	C_2	C_3	C_4
Omens et al. (1993)	1.2	26.7	2.0	14.7
Augenstein et al. (2005)	3.0	11.1	1.76	10.0
Current study	0.831	14.3	4.49	0.762

Author Manuscript

Author Manuscript

Author Manuscript

Author Manuscript